Supplementary Material (ESI) for Chemical Communications

Irreversible Solvent-Driven Conversion in Cyanometalate $\{Fe_2Ni\}_n$ (n = 2, 3) Single-Molecule Magnets

Yuan-Zhu Zhang,[a] Uma P. Mallik,[a] Rodolphe Clérac,[*c,d] Nigam P. Rath,[a] and Stephen M. Holmes*[a,b]

[a] Department of Chemistry & Biochemistry, University of Missouri-St. Louis, St. Louis, MO 63121, USA
[b] Center for Nanoscience, University of Missouri-St. Louis, St. Louis, MO 63121, USA
[c] CNRS, UPR 8641, Centre de Recherche Paul Pascal (CRPP), Equipe "Matériaux Moléculaires Magnétiques", 115 avenue du Dr. Albert Schweitzer, Pessac, F-33600, France
[d] Université de Bordeaux, UPR 8641, Pessac, F-33600, France

Experimental Section.

Materials. All operations were conducted under an argon atmosphere using standard Schlenk and dry box techniques. Transfers of solutions containing cyanide were carried out through stainless steel cannulas. Solvents were distilled under dinitrogen from sodium-benzophenone (diethyl ether) or magnesium turnings (methanol) and sparged with argon prior to use. DMF (Baker) was dried using activated alumina columns. The preparation of $[NEt_4][(Tp^{*Me})Fe(CN)_3]\cdot H_2O$ is described elsewhere.[1]

Physical Measurements. The IR spectra were recorded as Nujol mulls between KBr plates on a Nicolet 6700 FTIR instruments. Magnetic measurements were conducted on a Quantum Design MPMS XL magnetometer. Diamagnetic corrections were estimated using Pascal's constants.[2] Microanalyses were performed by Robertson Microlit Laboratories.

Structure Determinations and Refinements. X-ray diffraction data for **1** and **2** were obtained on a Bruker Apex II difractometer using Mo Kα radiation. Crystals were mounted in Paratone-N oil on glass fibers. Initial cell parameters were obtained (DENZO)[3] from ten 1º frames (SCALEPACK).[3] Lorentz/polarization corrections were applied during data reduction. The structures were solved by direct methods (SHELXL97)[4] and completed by difference Fourier methods (SHELXL97).[3] Refinement was performed against F^2 by weighted full-matrix least-squares (SHELXL97),[4] and empirical absorption corrections (either SCALEPACK[3] or SADABS[5]) were applied. Hydrogen atoms were found in difference maps and subsequently placed at calculated positions using suitable riding models with isotropic displacement parameters derived from their carrier atoms. Non-hydrogen atoms were refined with anisotropic displacement parameters. Atomic scattering factors were taken from the *International Tables for Crystallography Vol. C*.[6] Crystal data, relevant details of the structure determinations, and selected geometrical parameters are provided in Tables S1 and S2 (for **1** and **2**).

[1] Zhang, Y.-Z.; Mallik, U. P.; Rath, N.; Yee, G. T.; Clérac, R.; Holmes, S. M. *Chem. Commun.* **2010**, *39*, 5500-5503.
[2] Boudreaux, E. A.; Mulay, L. N. *Theory and Applications of Molecular Paramagnetism*; Wiley: New York, 1976.
[3] Otwinowski, Z.; Minor, W. *Methods Enzymol.* **1997**, *276*, 307-326.
[4] Sheldrick, G. M. *SHELX-97. Programs for Crystal Structure Solution and Refinement*; University of Gottingen: Gottingen, Germany, 1997.
[5] Sheldrick, G. M. *SADABS*s *An empirical absorption correction program*; Bruker Analytical X-ray Systems: Madison, WI, 1996.
[6] *International Tables for Crystallography Vol. C*; Kluwer Academic Publishers: Dordrecht, The Netherlands, 1992.

Table S1. Crystallographic Data for $\{[(Tp^{*Me})Fe^{III}(CN)_3]_4[Ni^{II}(DMF)_3]_2\}\cdot 4DMF\cdot H_2O$ (**1**) and $\{[Tp^{*Me})Fe^{III}(CN)_3]_6[Ni^{II}_3(MeOH)_8]_3\}\cdot 3H_2O\cdot 8MeOH$ (**2**).

cmpd.	**2**	**3**
crystal color	dark red	dark red
crystal shape	block	plate
crystal size, mm	0.15 × 0.12 × 0.08	0.40 × 0.30 × 0.14
formula	$C_{114}H_{182}B_4Fe_4N_{46}Ni_2O_{11}$	$C_{142}H_{235}B_6Fe_6N_{54}Ni_3O_{17.5}$
formula wt, g mol^{-1}	2757.12	3554.92
crystal system	triclinic	monoclinic
space group	$P\bar{1}$	$C2/c$
wavelength, Å	0.71073	0.71073
a, Å	12.142(2)	27.457(2)
b, Å	17.379(2)	17.275(1)
c, Å	17.500(2)	39.602(2)
α, °	102.334(5)	90
β, °	108.050(5)	95.747(3)
γ, °	94.584(5)	90
V, Å^3	3387.4(6)	18690(2)
Z	2	8
ρ_{calcd}, mg m^{-3}	1.352	1.263
μ, mm^{-1}	0.762	0.815
R_1[b]	0.0484	0.0681
wR_2[c]	0.0948	0.1804

[a] $I \geq 2\sigma(I)$. [b] $R1 = \sum||F_o| - |F_c||/\sum|F_o|$. [c] $wR2=\{\sum[w(F_o^2-F_c^2)^2]/ \sum[w(F_o^2)^2]\}^{1/2}$

Table S2. Selected Bond Distances (Å) and Angles (°) for **1** and **2**.

1						**2**				
Fe1-C1	1.910(4)		C1-Fe1-C2	86.5(2)		Fe1-C1	1.918(5)		C1-Fe1-C2	93.4(2)
Fe1-C2	1.927(5)		C1-Fe1-C3	85.6(2)		Fe1-C2	1.928(5)		C1-Fe1-C3	81.5(3)
Fe1-C3	1.927(4)		C2-Fe1-C3	85.4(2)		Fe1-C3	1.920(5)		C2-Fe1-C3	85.9(2)
Fe1-N8	2.004(3)		C1-Fe1-N8	92.4(1)		Fe1-N11	1.988(4)		C1-Fe1-N11	90.6(2)
Fe1-N10	1.997(3)		C1-Fe1-N10	94.2(2)		Fe1-N13	1.977(4)		C1-Fe1-N13	178.7(2)
Fe1-N12	2.001(3)		C1-Fe1-N12	94.2(1)		Fe1-N15	1.977(4)		C1-Fe1-N15	175.7(2)
Fe2-C4	1.927(4)		Fe1-C1-N1	175.3(3)		Fe2-C4	1.920(5)		Fe1-C1-N1	176.6(6)
Fe2-C5	1.920(4)		C4-Fe2-C5	98.5(2)		Fe2-C5	1.920(8)		Fe1-C2-N2	174.4(4)
Fe2-C6	1.901(4)		C4-Fe2-C6	91.0(2)		Fe2-C6	1.912(5)		C4-Fe2-C5	85.9(2)
Fe2-N14	1.986(3)		C5-Fe2-C6	85.4(2)		Fe2-N17	1.986(5)		C4-Fe2-C6	91.2(2)
Fe2-N16	1.983(3)		C4-Fe2-N14	89.6(1)		Fe2-N19	1.997(4)		C5-Fe2-C6	82.2(2)
Fe2-N18	2.000(3)		C4-Fe2-N16	99.0(1)		Fe2-N21	1.991(4)		C4-Fe2-N17	90.7(2)
Ni1-N1	2.068(3)		C4-Fe2-N18	178.1(1)		Fe3-C7	1.921(5)		C4-Fe2-N19	88.2(2)
Ni1-N4	2.039(3)		Fe2-C4-N4	172.9(3)		Fe3-C8	1.903(5)		C4-Fe2-N21	178.1(2)
Ni1-N6	2.001(3)		Fe2-C6-N6	176.4(3)		Fe3-C9	1.930(5)		Fe2-C4-N4	175.7(4)
Ni1-O1	2.079(2)		N1-Ni1-N4	178.8(1)		Fe3-N23	1.985(4)		Fe2-C6-N6	177.4(7)
Ni1-O2	2.059(2)		N1-Ni1-N6	93.9(1)		Fe3-N25	1.995(4)		C7-Fe3-C8	83.1(2)
Ni1-O3	2.100(3)		N1-Ni1-O1	88.0(1)		Fe3-N27	2.004(4)		C7-Fe3-C9	87.5(2)
			N1-Ni1-O2	90.9(1)		Ni1-N1	2.024(5)		C8-Fe3-C9	88.1(2)
			N1-Ni1-O3	88.4(1)		Ni1-N6	2.020(5)		C8-Fe3-N23	90.9(2)
			O2-Ni1-O3	88.1(1)		Ni1-O1	2.151(6)		C8-Fe3-N25	93.2(2)
			Ni1-N1-C1	170.2(3)		Ni1-O2	2.108(7)		C8-Fe3-N27	177.0(2)
			Ni1-N4A-C4A	177.1(3)		Ni2-N2	2.015(4)		Fe3-C8-N8	174.6(5)
			Ni1-N6-C6	171.6(3)		Ni2-N4	2.031(4)		N1-Ni1-N6	89.1(2)
			Fe2···Fe2A	6.9(3)		Ni2-N8	2.025(4)		N1-Ni1-O1	75.2(3)
			Ni1···Ni1A	7.5(3)		Ni2-O3	2.126(4)		N1-Ni1-O2	84.2(3)
			Fe1···Fe1A	17.0(3)		Ni2-O4	2.107(4)		O1-Ni1-O2	172.2(3)
						Ni2-O5	2.082(4)		Ni1-N1-C1	168.6(6)
						Ni1···Ni2	7.449(4)		Ni1-N6-C6	168.9(8)
						Fe1···Fe1A	6.903(4)		N2-Ni2-N4	88.1(2)
						Fe2···Fe2A	16.993(4)		N2-Ni2-N8	176.8(2)
									N4-Ni2-N8	91.6(2)
									O3-Ni2-O4	83.2(2)
									O3-Ni2-O5	170.1(2)
									O4-Ni2-O5	87.0(2)
									Ni2-N2-C2	170.0(4)
									Ni2-N4-C4	172.7(4)
									Ni1···Ni2	7.4(5)
									Fe1···Fe1A	6.9(6)
									Fe2···Fe2A	6.9(6)
									Ni2···Ni2A	14.8(6)
									Fe3···Fe3A	23.0(6)

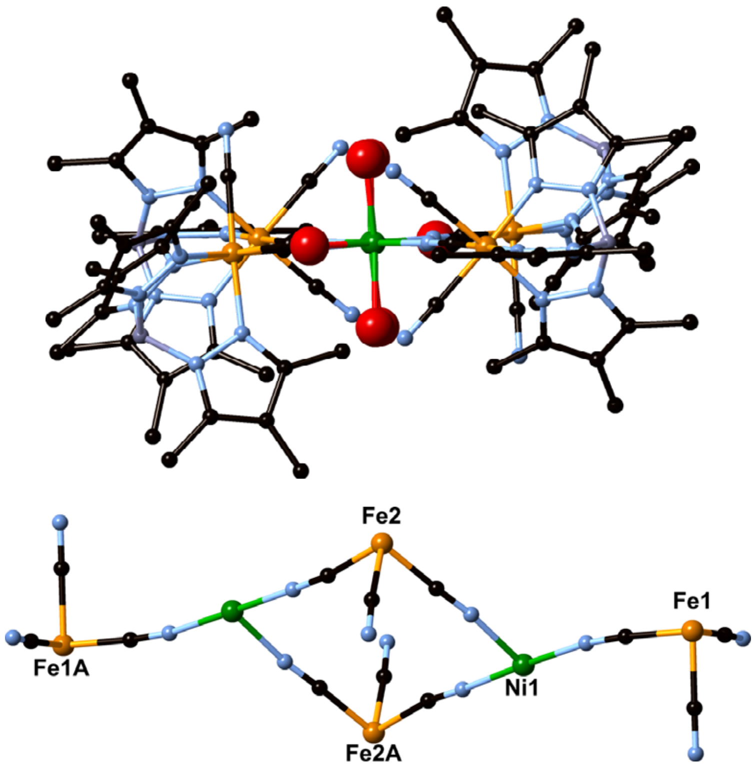

Fig. S1. (top) View of truncated and flat core present in **1** along the Ni···Ni vector. (bottom) View of complex core present in **1**.

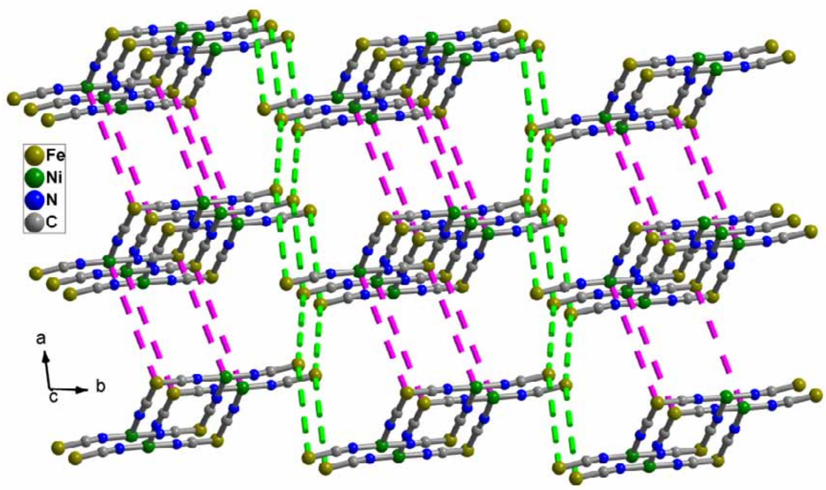

Fig. S2. Truncated packing arrangement of hexanuclear cores present in **1** with closest inter-complex metal-metal distance of 8.71(1) Å for Fe···Ni and 9.04(3) Å for Fe···Fe.

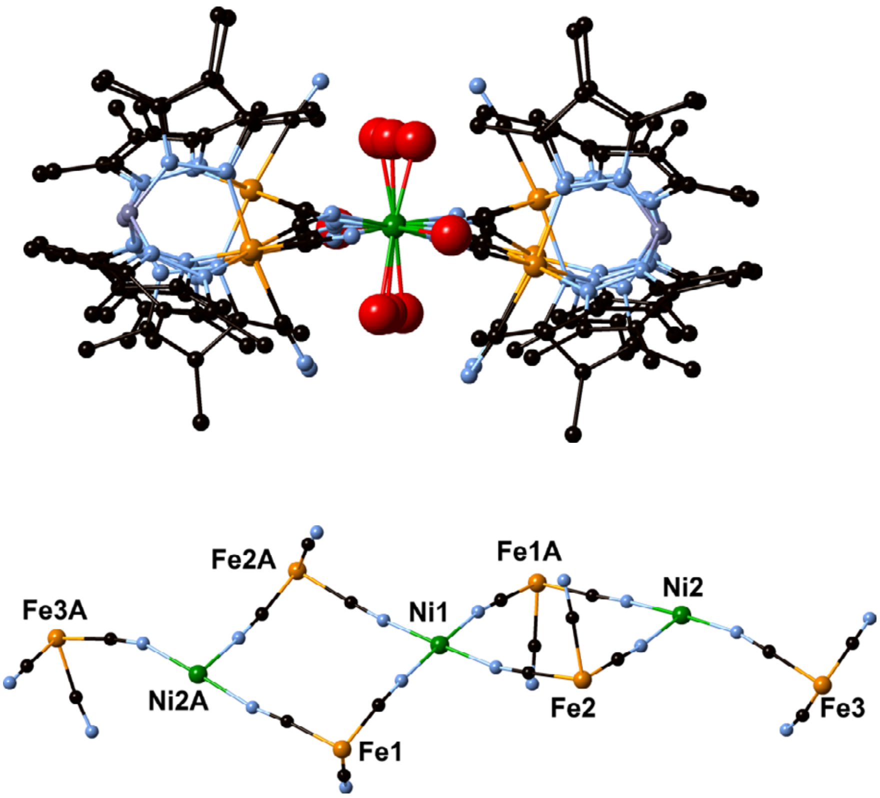

Fig. S3. (top) View of truncated and twisted core present in **2** along the Ni···Ni···Ni vector. (bottom) View of complex core present in **2**.

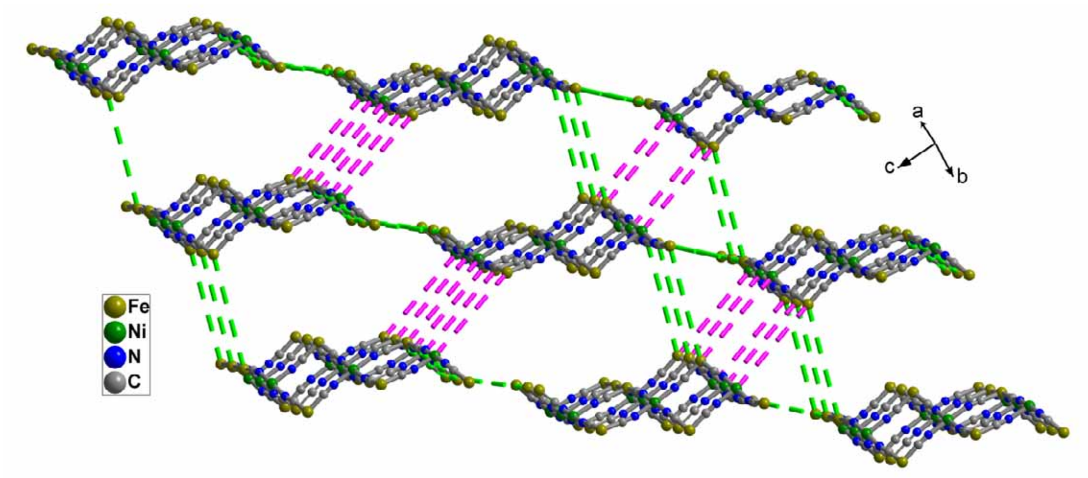

Fig. S4. Truncated packing arrangement of nonanuclear cores present in **2** with closest inter-complex metal-metal distance of 10.13(1) Å for Fe···Ni and 9.26(1) Å for Fe···Fe.

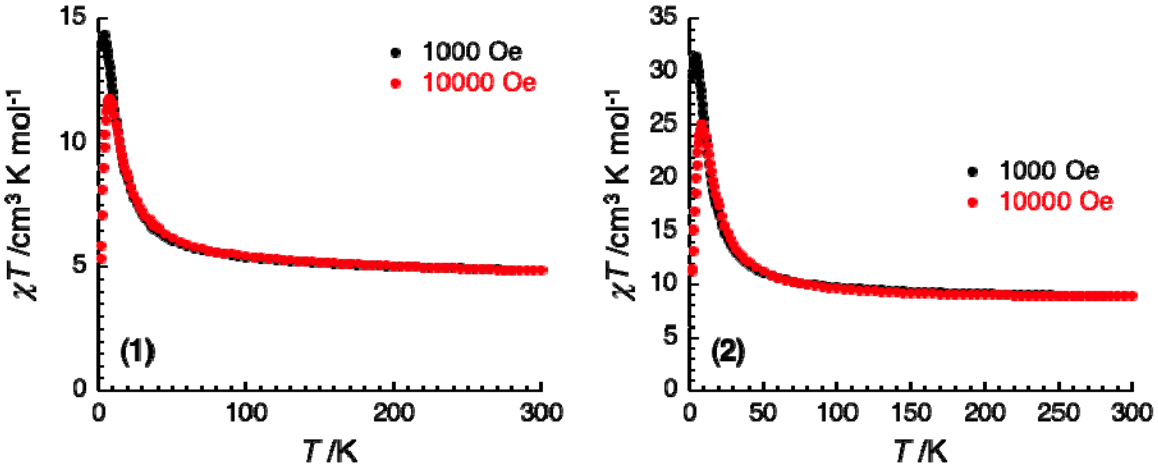

Fig. S5. Temperature dependences of the χT products (with χ defined as the magnetic susceptibility and equal to M/H) for H_{dc} = 1000 (•) and 10000 Oe (•) for **1** (left) and **2** (right).

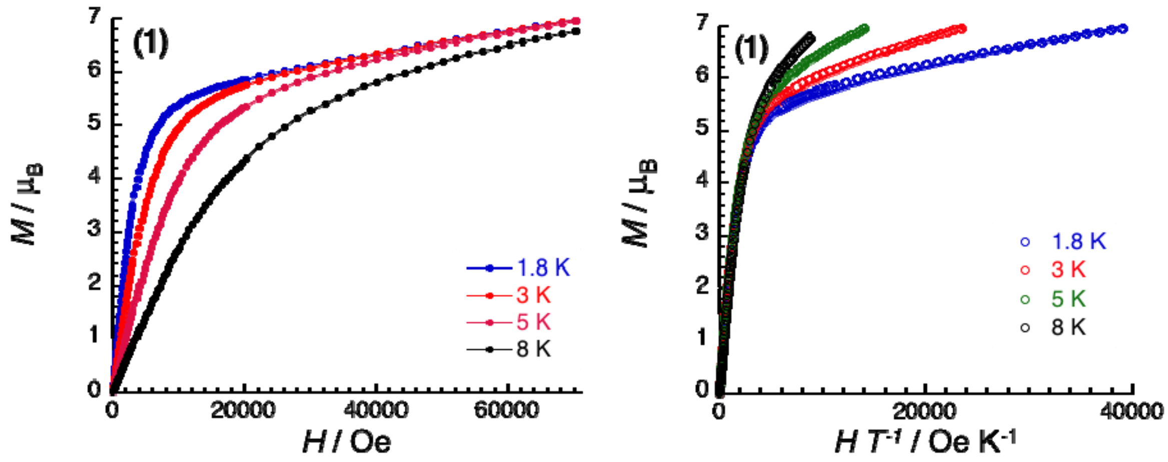

Fig. S6. *M* vs *H* (left) and *M* vs *H/T* (right) data for **1** below 8 K. The solid lines are guides for the eyes on the left plot but are on the right plot the best fits obtained with a S_T = 4 macro-spin model with D/k_B = -6.7 K and g = 2.65.

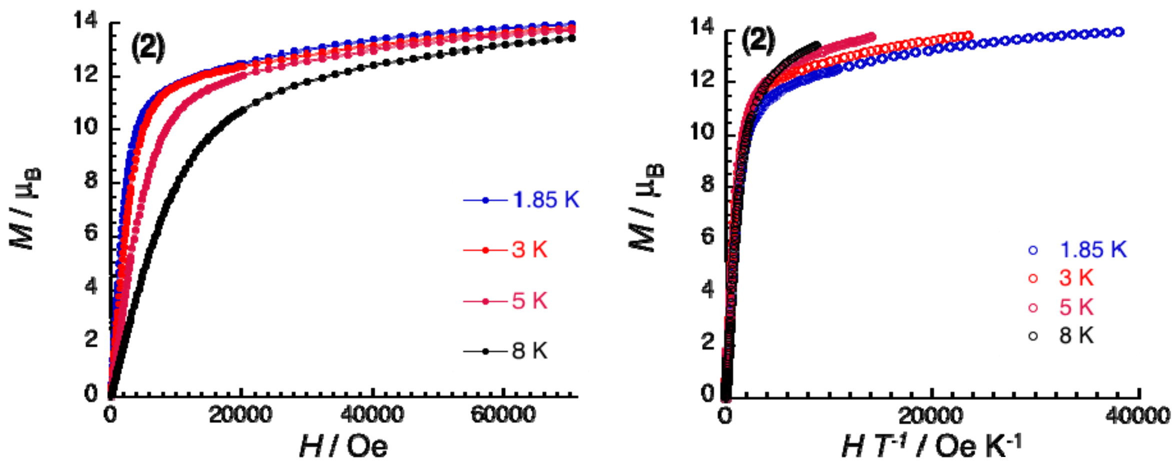

Fig. S7. *M* vs *H* (left) and *M* vs *H/T* (right) data for **2** below 8 K. The solid lines are guides for the eyes.

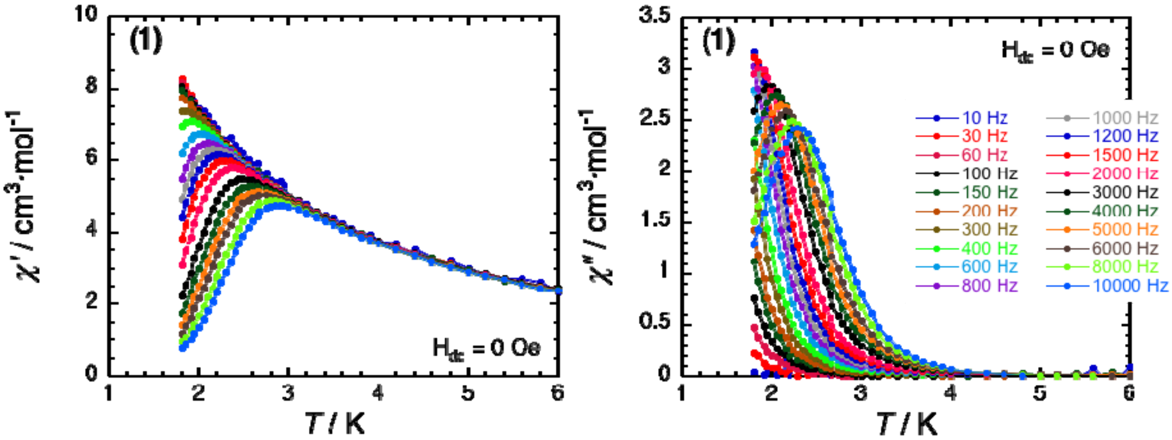

Fig. S8. Temperature dependence of the in-phase (left) and out-of-phase (right) components of the ac susceptibility between 10 and 10000 Hz (with H_{ac} = 1 Oe and H_{dc} = 0 Oe) for **1** below 6 K. The solid lines are guides for the eyes.

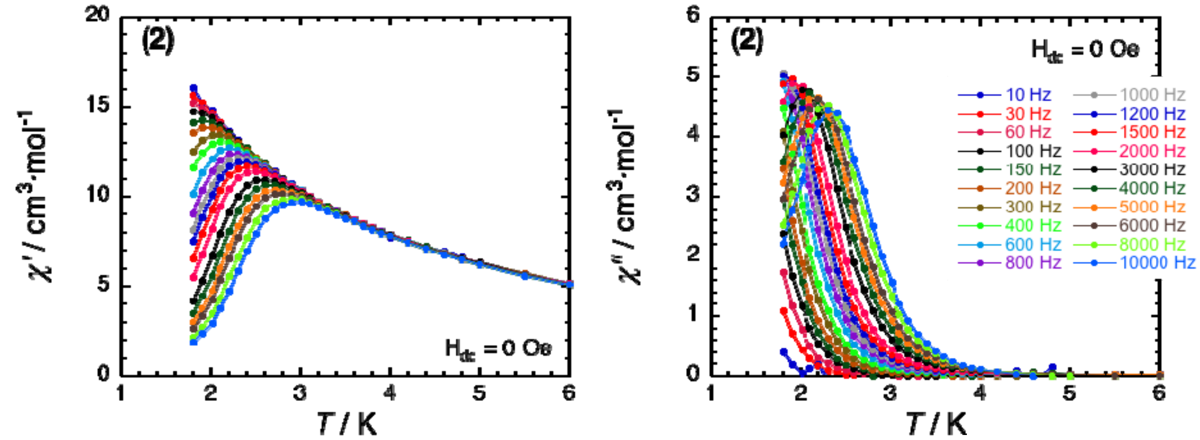

Fig. S9. Temperature dependence of the in-phase (left) and out-of-phase (right) components of the ac susceptibility between 10 and 10000 Hz (with H_{ac} = 1 Oe and H_{dc} = 0 Oe) for **2** below 6 K. The solid lines are guides for the eyes.

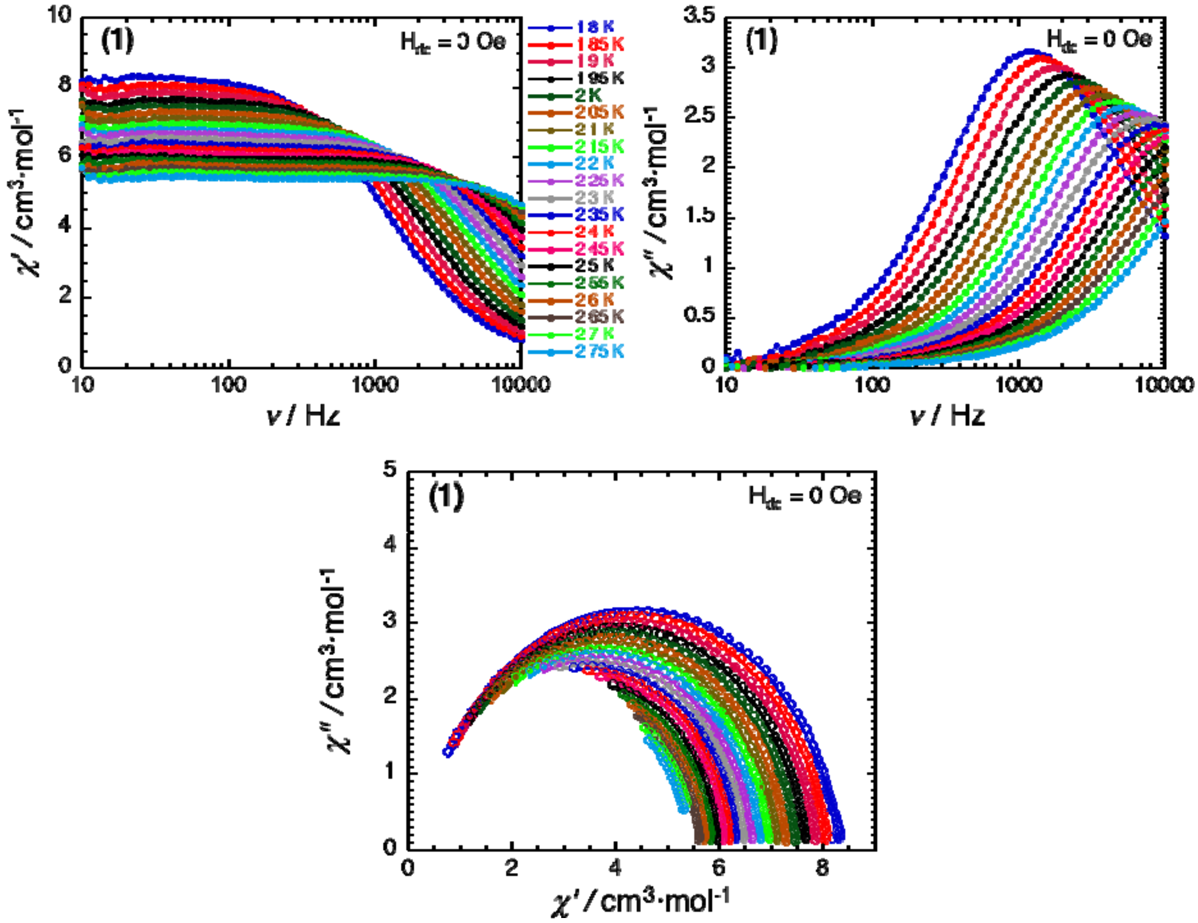

Fig. S10. Frequency dependence of the in-phase (top left) and out-of-phase (top right) components of the ac susceptibility at different temperatures between 1.8 and 2.75 K (with H_{ac} = 1 Oe and H_{dc} = 0 Oe) for **1**. The solid lines are guides for the eyes. Cole-Cole plots (bottom) at different temperatures between 1.8 and 2.75 K (with H_{ac} = 1 Oe and H_{dc} = 0 Oe) for **1**, the solid lines are the best fits to a generalized Debye model with α between 0.05 (2.6 K) and 0.15 (at 1.8 K).

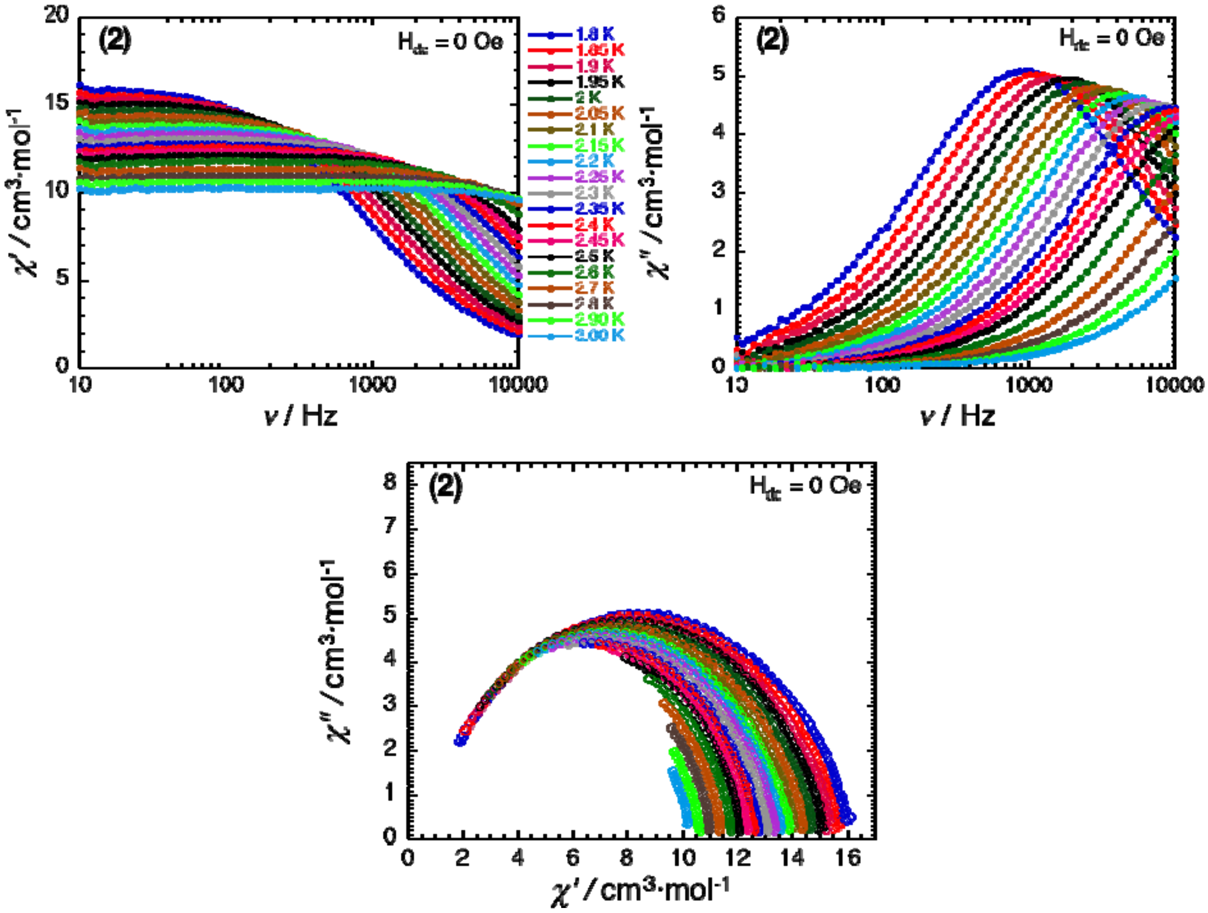

Fig. S11. Frequency dependence of the in-phase (top left) and out-of-phase (top right) components of the ac susceptibility at different temperatures between 1.8 and 3 K (with H_{ac} = 1 Oe and H_{dc} = 0 Oe) for **2**. Cole-Cole plots (bottom) at different temperatures between 1.8 and 3 K (with H_{ac} = 1 Oe and H_{dc} = 0 Oe) for **2**, the solid lines are the best fits to a generalized Debye model with α between 0.06 (2.7 K) and 0.26 (at 1.8 K).

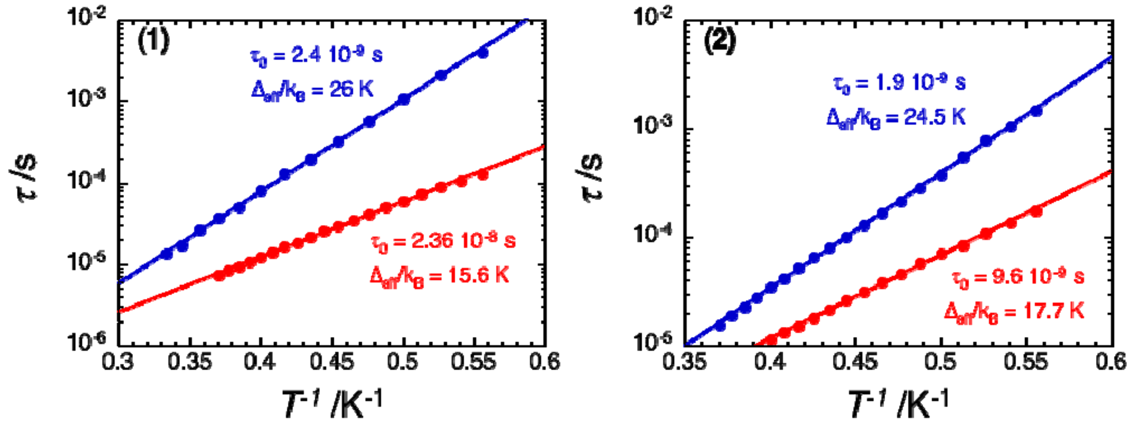

Fig. S12. (left) Semi-logarithmic τ vs $1/T$ plot from the frequency dependence of the ac susceptibility at H_{dc} = 0 Oe (•) and H_{dc} = 1500 Oe (•) for **1**. (right) Semi-logarithmic τ vs $1/T$ plot from the frequency dependence of the ac susceptibility at H_{dc} = 0 Oe (•) and H_{dc} = 600 Oe (•) for **2**. The solid lines are the best fits with Arrhenius laws.

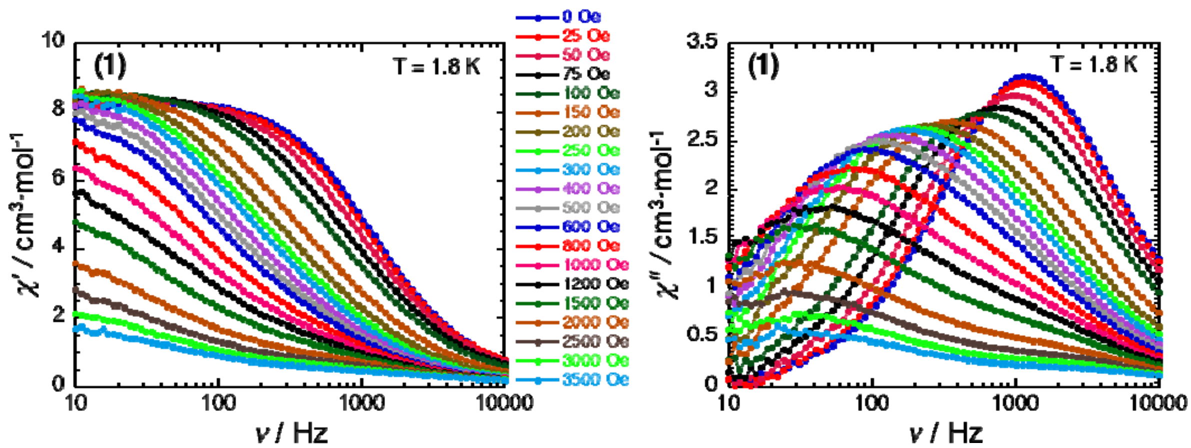

Fig. S13. Frequency dependence of the in-phase (left) and out-of-phase (right) components of the ac susceptibility at different applied dc fields between 0 and 3500 Oe (with H_{ac} = 1 Oe) for **1** at 1.8 K. The solid lines are guides for the eyes.

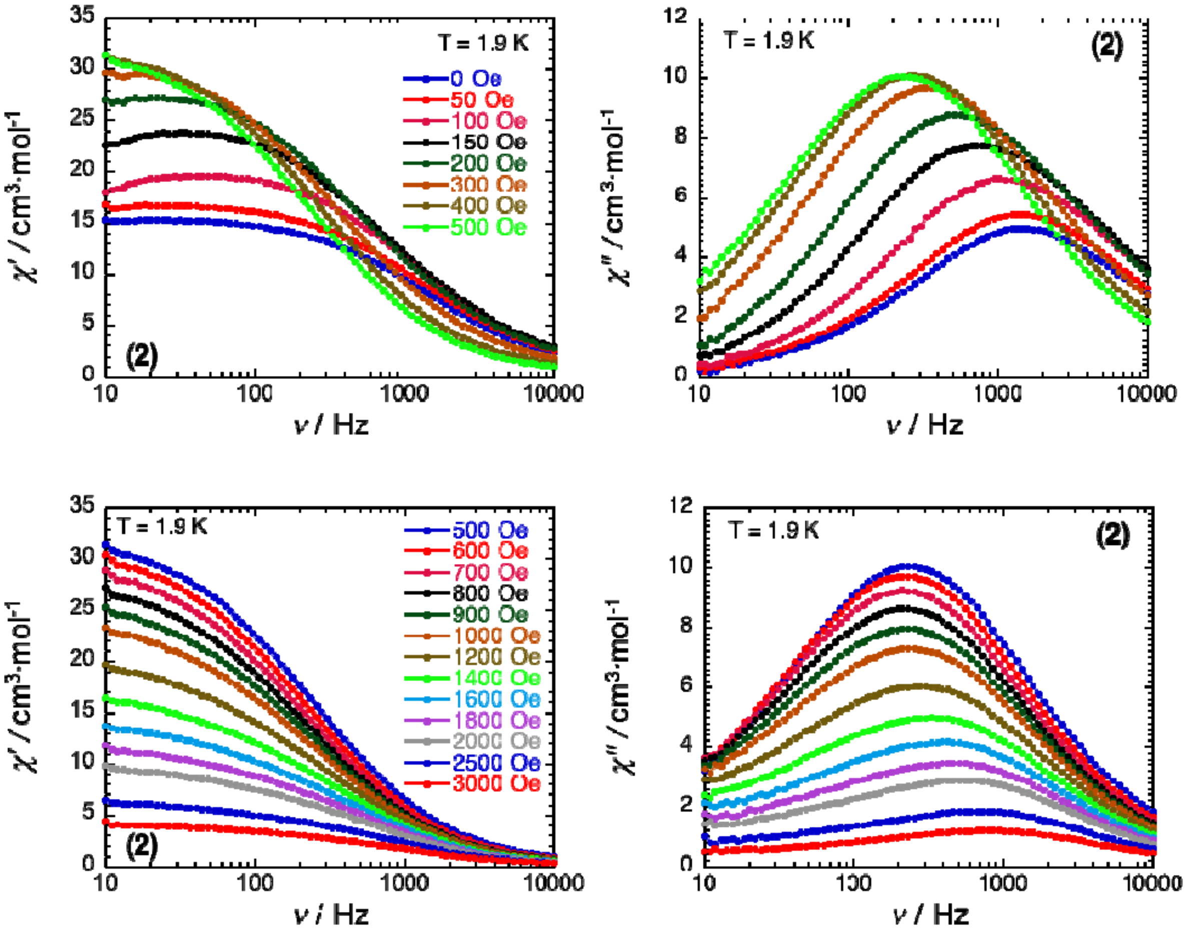

Fig. S14. Frequency dependence of the in-phase (left plots) and out-of-phase (right plots) components of the ac susceptibility at different applied dc fields for **2** at 1.9 K: top, between 0 and 500 Oe (H_{ac} =1 Oe); bottom, between 500 and 3000 Oe (H_{ac} =1 Oe). The solid lines are guides for the eyes.

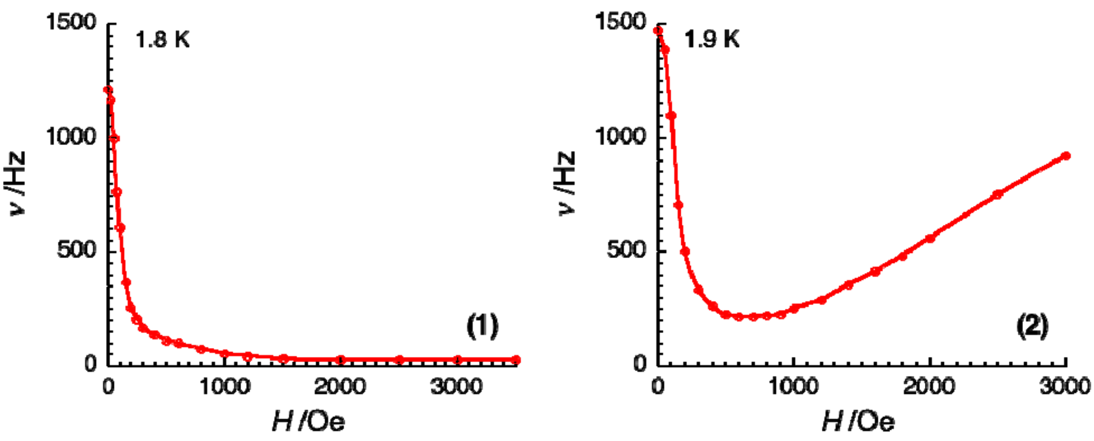

Fig. S15. (left) Field dependence of the characteristic frequency of the relaxation mode at 1.8 K for **1** deduced from Fig. S13. (right) Field dependence of the characteristic frequency of the relaxation mode at 1.9 K for **2** deduced from Fig. S14. The solid lines are guides for the eyes.

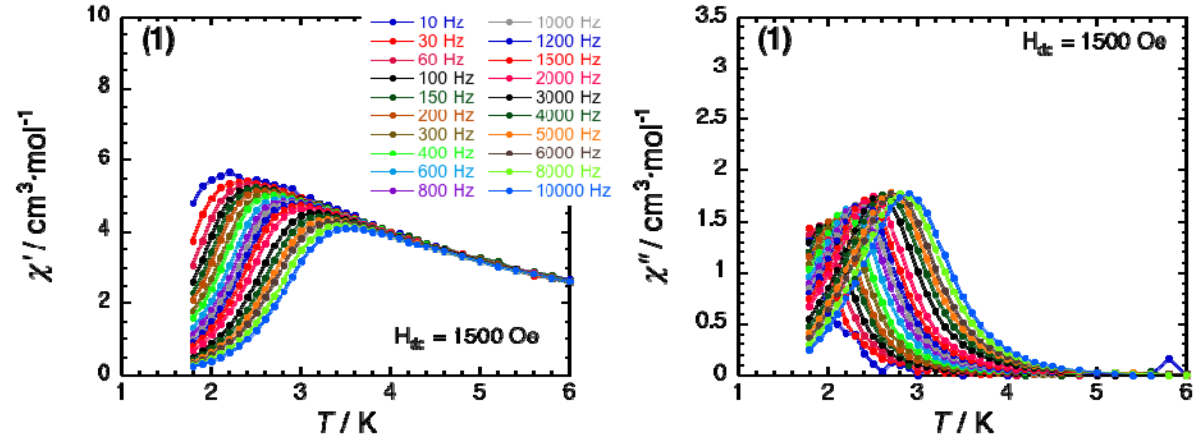

Fig. S16. Temperature dependence of the in-phase (left) and out-of-phase (right) components of the ac susceptibility between 10 and 10000 Hz (with H_{ac} = 1 Oe; H_{dc} = 1500 Oe) for **1** below 6 K. The solid lines are guides for the eyes.

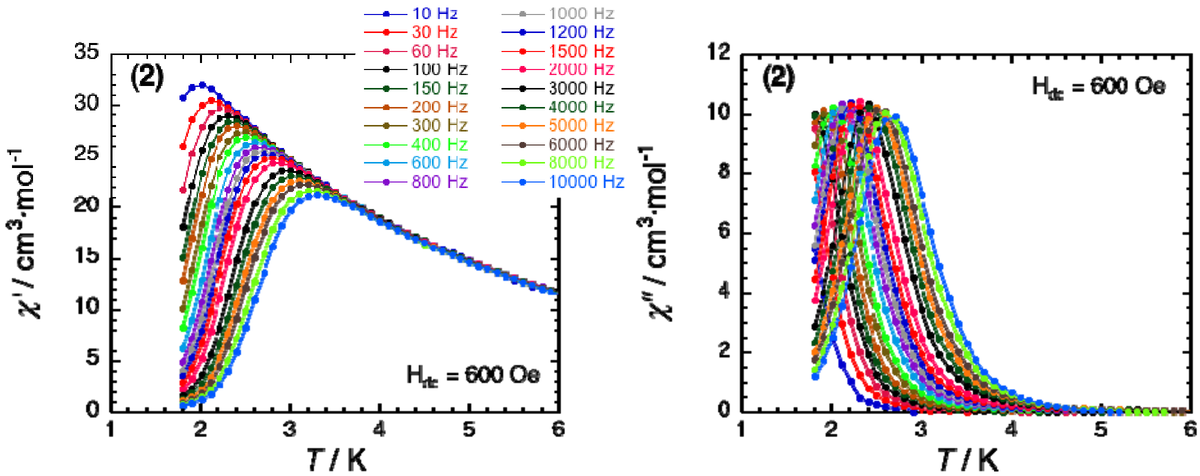

Fig. S17. Temperature dependence of the in-phase (left) and out-of-phase (right) components of the ac susceptibility between 10 and 10000 Hz (with H_{ac} = 1 Oe; H_{dc} = 600 Oe) for **2** below 5 K. The solid lines are guides for the eyes.

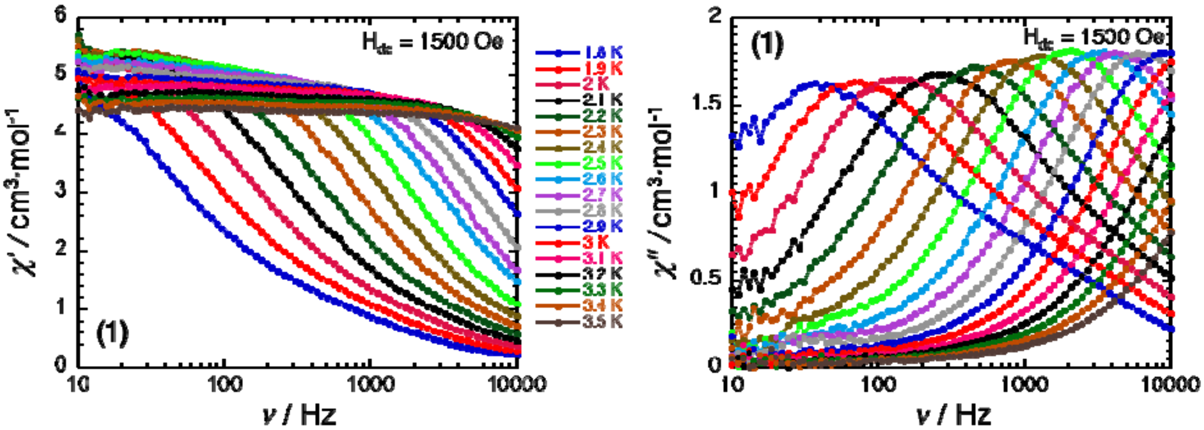

Fig. S18. Frequency dependence of the in-phase (left) and out-of-phase (right) components of the ac susceptibility at different temperatures between 1.8 and 3.5 K (with H_{ac} = 1 Oe; H_{dc} 1500 Oe) for **1**. The solid lines are guides for the eyes.

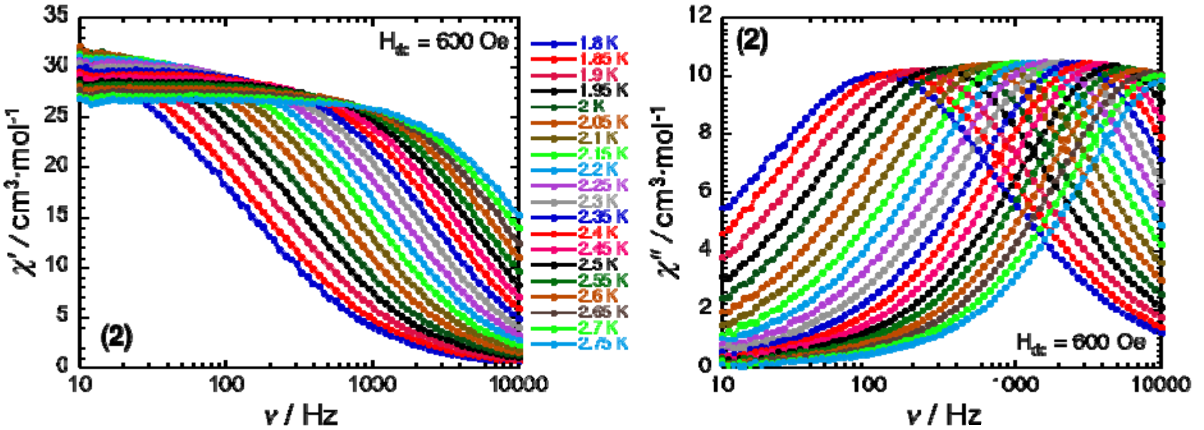

Fig. S19. Frequency dependence of the in-phase (left) and out-of-phase (right) components of the ac susceptibility at different temperatures between 1.8 and 2.75 K (with H_{ac} = 1 Oe; H_{dc} = 600 Oe) for **2**. The solid lines are guides for the eyes.